Check for updates

Untangling cation and anion contributions to refractive index changes in electrical double-layer capacitors

Karen Regules-Medel, [ID] Finlay Nelson,† William Hardiman,†
Rafael Fuentes-Domínguez, [ID] Michael G. Somekh and Sidahmed Abayzeed [ID] *

Label-free optical microscopy and sensing techniques are gaining attention for investigating electro-chemical reactions – critical for batteries, fuel cells, corrosion, chemical sensing, and bioelectrochemistry. Several studies have examined how perturbations of electrical double layer capacitors (EDLCs) affect the refractive index at metal–electrolyte interfaces and the consequent sensor output. However, the individual contributions of cations and anions to the overall optical response remain unexplored. We address this gap using coupled electrostatics and electrodiffusion models to simulate the metal–electrolyte interface, with resulting ion concentration profiles used to compute refractive index changes. We develop a mathematical model based on the Lorenz–Lorentz equation to estimate macroscopic refractive index changes using the concentration and molar refractivity of ions. We demonstrate this effect computationally using three optical configurations: normal incidence reflection modulation (NIRM), surface plasmon resonance (SPR) with the Kretschmann–Raether configuration, and localised surface plasmon resonance (LSPR) *via* gold nanoparticles. Each method exhibits sensitivity to refractive index variations due to excess or depletion of cations and anions. For a 1 : 1 sodium chloride electrolyte, we observe an asymmetric optical response upon polarity switching, with enhanced sensitivity at positive potentials due to chloride ions' higher molar refractivity relative to sodium ions. The response increases in inverse proportion to the optical field penetration depth at the sensing interface. These findings inform the design of highly sensitive optical sensors and offer insight into ion dynamics in biological systems, battery charge transport, and metrology of the optical properties of ionic species.

Introduction

Electrochemical phenomena have been the subject of intensive research for decades, shaping our understanding of systems involving electron transfer between chemical species. These advances have driven key technological developments in batteries,[1] fuel cells,[2] catalysis[3] and corrosion prevention.[4] Electrochemical processes occurring at electrode–electrolyte interfaces have also enabled investigation of ion dynamics that underpin electrical signalling in living systems.[5] In bioelectrochemistry, the role of redox reactions and electron transport in enzyme function has been thoroughly investigated,[6] thereby enabling the development of biofuel cells[7] and electrochemical biosensors.[8] Precise control of electrochemical processes has also led to the development of ion pumps capable of modulating cellular electrical behaviour, introducing a new class of implantable bioelectronic devices.[9–11] Additionally, electrochemical nanosystems have been created to probe[12] and alter cellular bioelectricity.[13] These systems can be activated using wireless electrochemistry techniques[14] to induce controlled redox-mediated apoptosis for cancer treatment.[15]

Traditionally, electrochemical processes are monitored through measurements of electrochemical potential, current, and impedance using precision electronic instrumentation. A range of electroanalytical techniques exist for this purpose, including scanning electrochemical microscopy (SECM),[16] three-electrode systems, and wireless bipolar electrochemical cells.[17] Alternatively, optical techniques[18–20] have emerged as complementary tools to monitor electrochemical activity, enhancing traditional electrical measurements.[21,22]

The integration of optical and electrochemical techniques, known collectively as spectroelectrochemistry,[23] has been explored since the 1970s. For instance, surface plasmon resonance (SPR) sensing has been used to study charge dynamics in the electrical double layer capacitor (EDLC) at gold–electrolyte interfaces,[24] while electroreflectance spectroscopy has probed

Optics and Photonics Research Group, University of Nottingham, Nottingham, UK.
E-mail: sidahmed.abayzeed2@nottingham.ac.uk
† These authors contributed equally.

This journal is © the Owner Societies 2026

Phys. Chem. Chem. Phys., 2026, **28**, 10853–10864 | 10853

various metal–electrolyte interfaces.[25–28] Recent developments have introduced plasmonic and non-plasmonic optical approaches for charge sensing and imaging.[29,30] The latter includes interferometric scattering for tracking ion dynamics in batteries[24] and optical transmission to observe charge modulation in field-effect transistors.[31] These advances now enable the study of electrochemical processes at the single-molecule level, with implications for super-resolution imaging of living cells.[32] More recently, label-free electrochemically modulated interferometric scattering has been introduced to image ion channel activity in live cells.[33]

This paper focuses on optical techniques designed to probe ion dynamics within the EDLC at the metal–electrolyte interface. The formation of this nanoscale capacitor is well known to occur at low voltages (± 200 mV). We have previously shown,[24] both theoretically and experimentally, that charging of the EDLC perturbs the free electron density within the Thomas–Fermi (TF) screening length of the metal surface. This effect induces a change in refractive index, which can be optically measured using SPR sensors.[24] Plasmonic sensors have been widely used to study perturbation of the EDLC,[20,24,29,34] generally assuming that changes occur within the TF region and neglecting the ionic contributions from the electrolyte. Non-plasmonic methods have also demonstrated sensitivity to refractive index changes near the interface. Faez and colleagues have developed a darkfield microscopy method to measure voltage-induced light modulation, which has been attributed to refractive index changes within the diffuse layer.[30,35,36] This approach motivates further investigation of the specific contributions of individual ionic species within the diffuse layer to the cumulative optical signal, an area that remains unexplored.

Theoretical framework

We introduce a theoretical framework to quantify the refractive index changes associated with different ionic species during the charging and discharging of the EDLC, focusing on the role of cation and anion concentrations. For a 1:1 electrolyte such as sodium chloride, one may expect a symmetric optical response for voltages of opposite polarity, if the charge is only considered. However, if the refractive indices of the ionic species differ, an asymmetric response may arise. To explore this effect, we apply the Lorenz–Lorentz equation,[37,38] which relates the macroscopic refractive index (n) to microscopic polarizability (α) and molar refractivity (R):

$$R = \frac{n^2 - 1}{n^2 + 2} \times \frac{1}{c} = \frac{4\pi}{3} N_A \alpha \tag{1}$$

here, c is the molar concentration (mol m^{-3}) of molecules interacting with light and N_A is Avogadro's number. At optical frequencies, α reflects the deformation of the electron cloud under the influence of the electric field, enabling estimation of the refractive index from the ionic concentration.[39]

Complex local-field models, such as the Kirkwood–Booth formalism, incorporate orientational correlations between permanent molecular dipoles and are essential for describing the static dielectric response of polar liquids. In the present work, however, the refractive index modulation is probed at optical frequencies and arises primarily from ionic concentration variations, such that the response is dominated by fast electronic polarisation. Under these conditions, Lorentz–Lorenz provides the appropriate leading-order description, with correlation-induced local-field effects expected to contribute only minor quantitative corrections.[40]

Eqn (1) assumes that the sample interacting with light is formed of homogeneous molecules. However, for a sample that is a mixture of different molecules or ionic species, as is the case in this paper, the additivity rule applies.[41] This rule states that the refractive index of the mixture is related to the sum of the molar refractivities (R_i) of its different components, weighted by their corresponding concentrations (c_i):

$$\frac{n^2 - 1}{n^2 + 2} = \sum_i R_i c_i \tag{2}$$

For cations and anions, molar refractivity has been calculated theoretically using a mathematical model derived by Pauling in 1927,[42] which employs a quantum mechanical approach under the assumption that ions exist in a gaseous state. The model has been validated experimentally, demonstrating the ability to predict the molar refractivity of ions in both gaseous and infinite dilution states. It should be noted that the additivity rule assumes that components within the mixture do not interact.[43] This assumption may have limitations in concentrated electrolyte solutions where ion–ion and ion–solvent interactions become significant.

Ion–ion interactions and ion–solvent interactions were considered by Pacak[39] in a study that measured the refractive index of different ionic solutions. These results were then compared to the theoretical refractive index of the ionic mixture that exists in a gaseous state or at infinite dilutions. The resulting deviation from the additivity rule is attributed to the alteration of polarizability induced by the solvent molecules or crystal formation. The combined theoretical and experimental approach resulted in tabulated values of molar refractivity for different anions and cations,[44] measured at a wavelength of 589.3 nm (sodium D-line). These values can be used to calculate the wavelength-dependent refractive index of ionic solutions and assess excess polarizability due to ion–ion and ion–solvent interactions.

The refractive index, at a distance x from the electrode, is influenced by the voltage-induced excess or deficiency of ions relative to the bulk concentration. When an external voltage is applied, the refractive index can be defined by

$$n(x) = n_{\text{bulk}} + \Delta n(x) \tag{3}$$

where n_{bulk} is the refractive index of the bulk solution at the equilibrium concentration. $\Delta n(x)$ denotes the voltage-induced deviation relative to the bulk, which can be determined using the change in ion concentration (Δc_i). The change in electrolyte refractive index n with respect to the concentration of each ion,

10854 | *Phys. Chem. Chem. Phys.*, 2026, **28**, 10853–10864

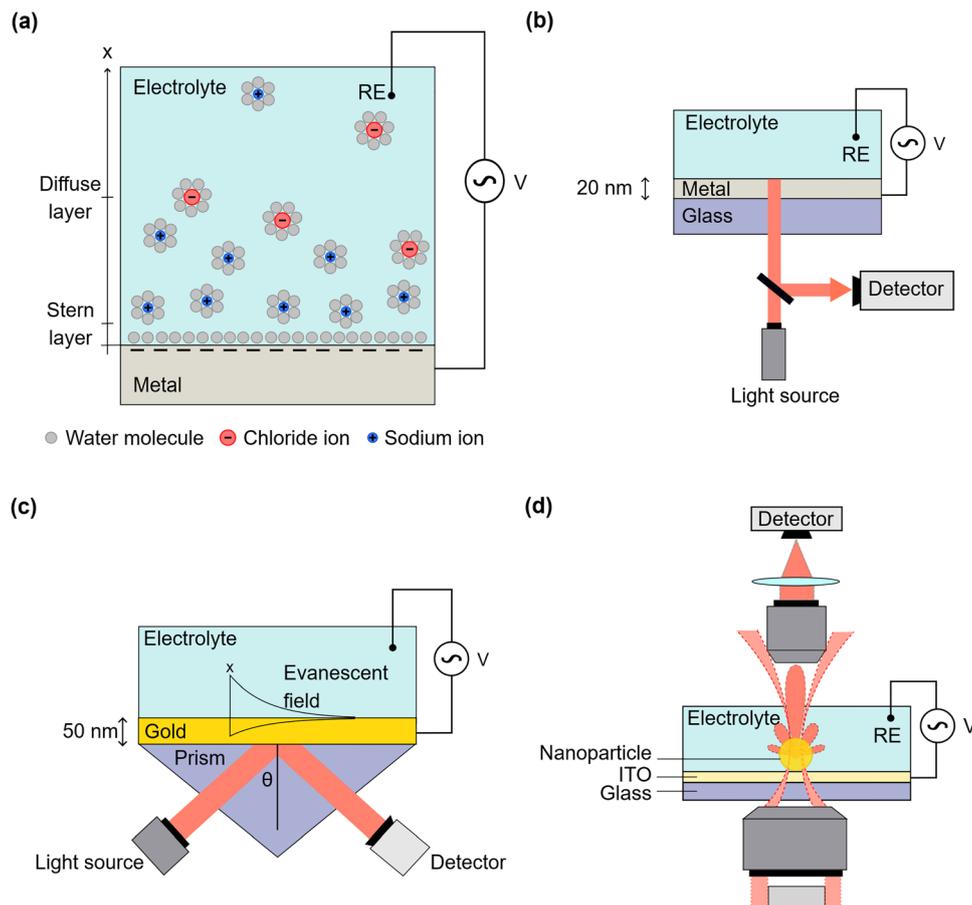This journal is © the Owner Societies 2026

Fig. 1 Optical probing of electrode–electrolyte interfaces. (a) Formation of the electrical double layer capacitor (EDLC) at the metal–electrolyte interface. (b)–(d) Optical configurations for normal-incidence reflection modulation (NIRM), surface plasmon resonance (SPR) and localised plasmon resonance (LSPR) sensing, respectively, used for sensing ion dynamics within the EDLC.

c_i, is expressed as

$$\Delta n = \sum_i \frac{\partial n}{\partial c_i} \Delta c_i(x) \qquad (4)$$

The molar refractivity of ions (R_i) can be used to estimate the corresponding change in refractive index with respect to the ion concentration ($\partial n/\partial c_i$), which is derived in Section S1 and summarized in eqn (5):

$$\frac{\partial n}{\partial c_i} = \beta R_i, \quad \beta = \frac{(n^2 + 2)^2}{6n} \qquad (5)$$

In this study, finite-element modelling is used to compute ion concentration profiles near the interface, which are then translated into refractive index profiles to simulate the response of various optical sensing techniques, as summarized in Fig. 1.

The theoretical framework presented above establishes the physical relationship between the concentration of ionic species and refractive index modulation within the electrical double layer. The numerical electrodiffusion modelling and optical simulations used to implement and evaluate this framework are described in the Methods section.

Key findings

This study compares refractive index changes within both the TF region (metal side) and the Debye layer (electrolyte side) at voltages of ± 200 mV. To place these findings in a broader context, we assess three optical techniques (Fig. 1b–d), with different optical penetration depths and sensitivities to refractive index changes. Specifically, we examine the following:

• Normal-incidence reflection modulation (NIRM) sensing, where the optical field has effectively an infinite penetration depth.

• Surface plasmon resonance (SPR) sensing using thin gold films where evanescent fields extend several hundred nanometres.[45]

• Localised plasmon resonance (LSPR) sensing using gold nanoparticles where decay lengths are a few tens of nanometres.[46]

Our investigations have revealed important findings related to optical sensing of EDLCs taking into account the differential molar refraction of ionic species at the electrode–electrolyte interface. A summary of these findings is provided below:

(a) Label-free plasmonic (SPR and LSPR) and non-plasmonic (such as NIRM, which does not rely on surface plasmon

This journal is © the Owner Societies 2026

Phys. Chem. Chem. Phys., 2026, **28**, 10853–10864 | **10855**

excitation) methods can detect voltage-induced refractive index changes due to ionic concentration dynamics within the diffuse layer.

(b) Refractive index changes within the TF region are symmetric with respect to voltage polarity, since such an effect is only driven by excess or deficiency of electrons. In contrast, changes in the diffuse layer yield asymmetric optical responses, attributed to differential molar refraction of cations and anions.

(c) Responsivity – defined as the resonance shift, or change in reflection, induced by changes in the diffuse layer's refractive index – increases as the penetration depth decreases. Accordingly, LSPR sensors exhibit the highest responsivity, followed by SPR and NIRM sensors.

Results and discussion

Electrodiffusion modelling of the electrode–electrolyte interface

We address a coupled problem that combines electrostatics and electrodiffusion to investigate the contributions of individual ionic species to voltage-induced changes in the optical properties of the metal–electrolyte interface. This modelling approach is well-established for studying charge carrier dynamics under electric fields across various geometries.[47,48]

The electrodiffusion model characterises the concentration dynamics of ionic species according to the Nernst–Planck equation:

$$\frac{\partial c_i}{\partial t}(x) = \nabla \cdot \left(D_i \nabla c_i(x) + F z_i \mu_i c_i(x) \vec{E}(x) \right) \qquad (6)$$

where c_i is the concentration of ion species i. The model can be independently solved for each species under the assumption of the dilute electrolyte approximation. The dynamics are governed by two physical effects:

1. Diffusion, described by the diffusion coefficient D_i and concentration gradient ∇c_i. This term corresponds directly to Fick's law of diffusion, which states that flux is proportional to the concentration gradient.

2. Drift, resulting from the electrophoretic mobility μ_i, ionic valency z_i, and the electric field $\vec{E}(x)$, where F is Faraday's constant.

We assume a strong electrolyte model, wherein the electrolyte is fully dissociated, and both sodium and chloride ions are present at physiological concentrations (150 mM). The model solves for the spatial profiles of both concentration and electrostatic potential, using prescribed boundary conditions on electrode potentials. The two fields are coupled using Poisson's equation:

$$\nabla \cdot \vec{D}(x) = \rho_v(x) \qquad (7)$$

where $\vec{D}$ is the electric displacement field and $\rho_v(x) = F \sum_i z_i c_i(x)$ is the local charge density derived from ion concentrations. Electrostatics thus links the applied surface potential and the system's dielectric properties to ionic behaviour, which is evaluated using the drift–diffusion framework, eqn (6). As a result, we can determine ion concentration fields under various voltage boundary conditions.

Together, eqn (6) and (7) constitute the Poisson–Nernst–Planck (PNP) mean-field description of ion transport and electrostatics; in the steady-state, zero-flux limit, this framework reduces to the classical Poisson–Boltzmann (PB) model.

To investigate ion dynamics in the diffuse layer and the associated changes in optical refractive index, we constructed a one-dimensional steady-state model, as shown in Fig. 2a, solving for equilibrium voltage and concentration profiles. The one-dimensional approach is valid for planar electrode configurations typically used in SPR voltage sensing[24] and NIRM systems.[49] Furthermore, it serves as a good approximation for metallic nanoparticles with radii significantly larger than the Debye length, as curvature effects are negligible for particles above ∼10 nm in diameter.[50] The model was implemented using COMSOL Multiphysics (version 6.1), employing both the electrostatics and transport of diluted species modules. From the simulations, we obtained the electric potential, electric field strength, and ionic concentration profiles. These parameters are shown in Fig. 2b, and they are consistent with
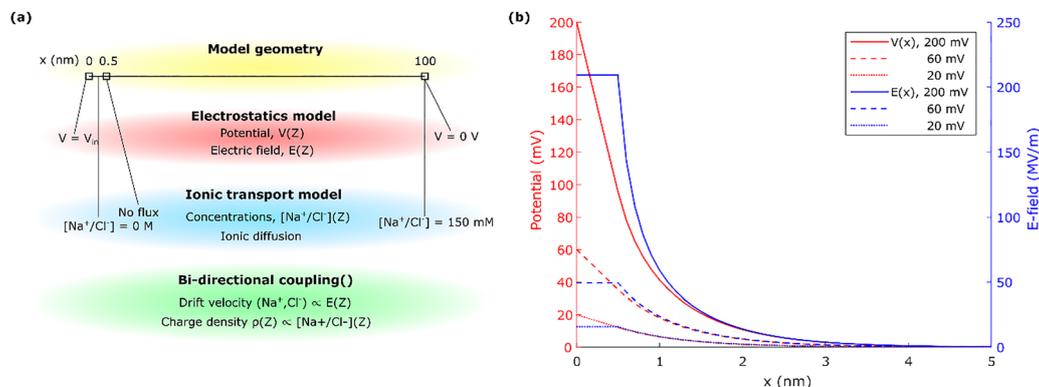

Fig. 2 Electrodiffusion modelling of the electrical double layer at the metal–electrolyte interface. (a) 1D half-cell model combining electrostatic effects and electrodiffusion of ionic species at the metal–electrolyte interface under external voltage perturbation. (b) Electric potential and electric field profiles at the metal–electrolyte interface.

10856 | *Phys. Chem. Chem. Phys.*, 2026, **28**, 10853–10864

This journal is © the Owner Societies 2026

the conventional Stern–Gouy–Chapman model of the EDLC, as discussed in Section S2. Finite-element modelling was chosen over analytical approaches since it is extensible to complex geometries.

The voltage and electric field profiles exhibit canonical behaviour of a double-layer capacitor: a relatively constant field in the compact Stern layer, followed by an exponential decay in the diffuse layer.[51] This modelling framework enables a detailed examination of how different cations and anions respond to applied voltages—an analysis presented in the following section.

Voltage-controlled refractive index changes in the diffuse layer

Understanding the optical properties of electrified metal–electrolyte interfaces is crucial. Such knowledge supports the development of novel optical microscopy techniques capable of revealing the spatial and temporal dynamics of electrochemical processes at the microscopic scale. Several optical methods, such as SPR microscopy and interferometric scattering microscopy (iSCAT), are highly sensitive to changes in the refractive index. For instance, SPR sensors can detect refractive index changes as small as 10^{-8} refractive index units (RIU).[52] Recent advances using machine learning algorithms[53] promise to further improve detection limits.[54,55] Similarly, iSCAT

techniques are capable of detecting nanoparticles,[56] single molecules[57] and single-protein dynamics.[58] Both methods have been explored as candidates for optical readout in electrochemical microscopy.[18–20,30]

To investigate the spatial distribution of refractive index changes induced by ion redistribution, we employ a one-dimensional multilayer model representing the metal–electrolyte interface. As illustrated in Fig. 3a, the metallic side consists of a bulk gold region and a TF screening layer. The TF layer describes the region within which free electrons in the metal respond to an applied surface potential, altering the local optical properties. Gold is selected as the model material due to its well-characterised plasmonic behaviour. On the electrolyte side, the interface is composed of the Stern layer with a thickness that is defined by the diameter of water molecules ($\sim$0.5 nm). This is followed by the Debye layer, where the potential decays to $1/e$ of the Stern potential. To assess whether ionic contributions beyond the Debye length are significant, we introduce an additional "sub-diffuse" layer of thickness equal to one Debye length. This extends the profile to the point where the potential has decayed to approximately $1/e^2$ ($\approx$14%) of its initial value at the end of the Stern layer. The purpose of this extra layer is purely analytical: it allows us to test whether
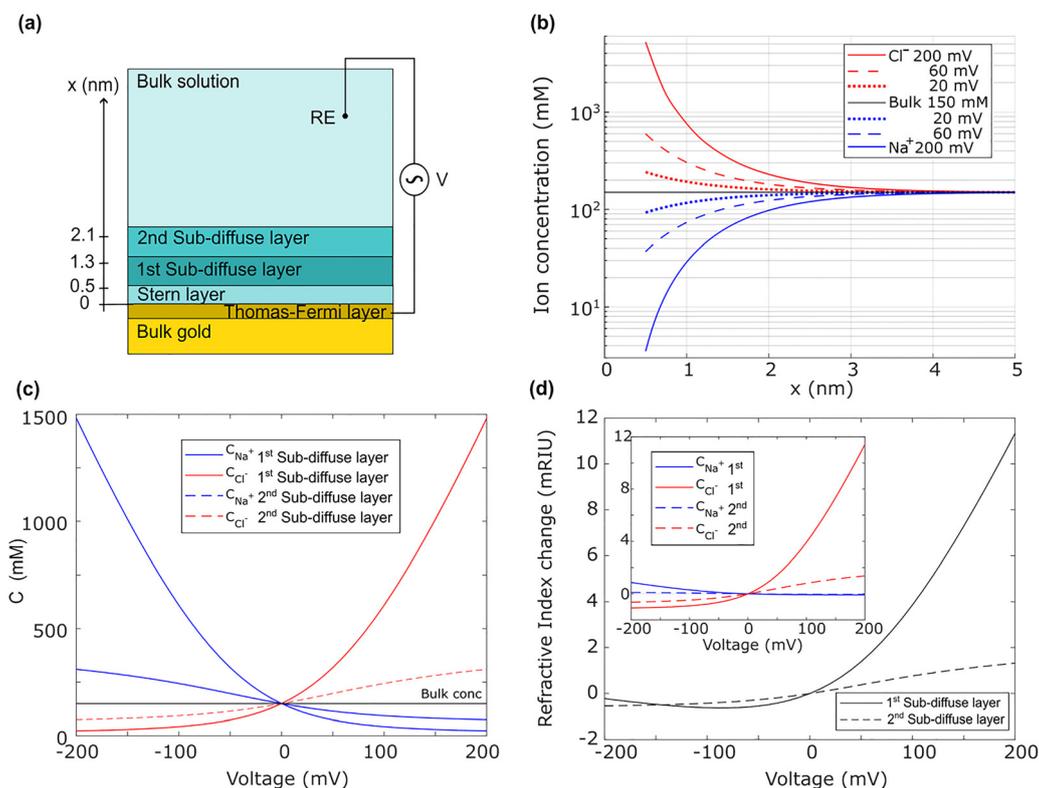

Fig. 3 Anion and cation concentrations and refractive index change profiles at the metal–electrolyte interface. (a) A 1D multilayer model of the metal–electrolyte interface; the gold thin film is divided into bulk and TF layers, while the electrolyte is divided into the Stern layer, Debye layer (1st sub-diffuse layer) and additional sub-diffuse layer before the bulk electrolyte region. (b) Spatial concentration profiles of sodium and chloride ions for exemplar surface potentials. (c) Average anion and cation concentrations for different voltage levels calculated for the Debye layer and the additional sub-diffuse layer. (d) Spatial refractive index profile resulting from the additive changes in concentrations of sodium and chloride ions at different voltages. The inset breaks down the contribution of the different segments of the diffuse layer (*i.e.*, 1st and 2nd sub-diffuse layers) decomposing the refractive index changes due to cations and anions.

This journal is © the Owner Societies 2026

Phys. Chem. Chem. Phys., 2026, **28**, 10853–10864 | **10857**

contributions from regions beyond one Debye length can be neglected or must be considered. In principle, the model could be generalised to n layers to describe the concentration as a function of distance, but here we employed two effective layers in addition to a semi-infinite electrolyte, for simplicity.

Fig. 3b shows the spatial concentration profiles of Na$^+$ and Cl$^-$ ions at the metal–electrolyte interface, computed using the electrostatics and electrodiffusion model described previously. The x-axis corresponds to the spatial coordinate of the 1-D layer model defined in Fig. 3a. Profiles are presented for externally applied positive voltages of 20, 60, and 200 mV. As the distance from the interface increases (x-axis), both concentrations asymptotically approach the bulk electrolyte value (150 mM), with chloride decreasing and sodium increasing exponentially. Although only positive voltages are shown in the main text, negative voltage behaviour is presented in Section S3 and displays symmetrical but polarity-inverted profiles, consistent with the behaviour expected for a symmetric 1:1 electrolyte. This SI section also shows the exact ion concentration at Stern for different voltages.

To quantify the contribution of each ionic species to the optical response, we computed the average ion concentrations across the two sublayers of the diffuse region (Fig. 3c). These averages are determined by integrating the concentration profile over the respective region and normalizing by the region's length. Specifically, the calculations are performed for two regions: the first sub-diffuse layer (Debye layer), covering the volume from 0.5 to 1.3 nm from the surface, and the second sub-diffuse layer, an additional region extending from 1.3 to 2.1 nm. The results show how average ion concentrations in these layers vary with applied voltage. In the first sublayer, the average concentration of sodium increases significantly for negative voltages, as ions are attracted towards the surface, reaching a concentration of 1480 mM at −200 mV. Conversely, for positive voltages, sodium ions are repelled, resulting in a concentration decrease, with values as low as 23 mM at +200 mV. At 0 V, the concentrations of anions and cations are the bulk concentration of 150 mM. Chloride ions show the opposite behaviour: they are repelled at negative voltages and attracted at positive voltages, mirroring the sodium concentrations. This reciprocal accumulation and depletion of counter-ions and co-ions is consistent with the Boltzmann distribution of ions in an electrostatic potential. For chloride, the concentration also reaches extreme values at ±200 mV, but with opposite signs compared to sodium. In the second sub-diffuse layer, the concentration variations are much smaller compared to the Debye layer, indicating that the effect of the applied voltage diminishes with the distance from the surface. For sodium, the concentrations at −200 mV and +200 mV are 310 mM and 23 mM, respectively, approximately five and three times smaller than those in the first sublayer.

The spatially resolved refractive index changes within the diffuse layer capacitor are shown in Fig. 3d, distinguishing between the Debye layer and the adjacent sub-diffuse region under varying surface potentials. Refractive index values were computed from the local ionic concentrations using the Lorenz–Lorentz formalism, as described in the Methods section.

Notably, the refractive index change in the Debye layer is, on average, approximately five times higher than that observed in the adjacent sub-diffuse layer. This observation confirms that the combined inclusion of these two regions is sufficient to capture the optically significant changes induced by ion redistribution, forming the basis for analysis of sensor response in the subsequent section.

A key result is the pronounced asymmetry in refractive index modulation between positive and negative voltage biases. Application of a positive surface potential results in a markedly larger refractive index increase compared to the corresponding decrease under a negative potential. This asymmetry arises from the disparity in molar refractivities of the involved ions: chloride ions possess a molar refractivity (8.57×10^{-6} m^3 mol^{-1}) approximately thirteen times greater than that of sodium ions (0.65×10^{-6} m^3 mol^{-1}).[59] As a result, at a positive voltage, the refractive index changes due to the accumulation of chloride in the diffuse layer exceed the refractive index change due to the depletion of sodium ions, which can be clearly observed from Fig. 3d. On the other hand, under negative potential, the deficiency of chloride ions has a higher effect in comparison to the excess of sodium ions, leading to a plateau as the voltage increases before returning to zero. With the knowledge of molar refractivity of ionic species, this approach can be used to compute the refractive index changes within the EDLC for different electrolyte solutions and predict the response of the different sensing techniques, as discussed in the following section.

While the main analysis focuses on a monovalent 1:1 NaCl electrolyte, the modelling framework is general and can be extended to charge-symmetric multivalent systems. As a demonstration, we include simulations for a 2:2 MgSO$_4$ electrolyte in the SI (Section S4), which show enhanced asymmetry and stronger diffuse-layer contributions consistent with increased ionic valence.

Modelling optical responses to refractive index changes at the metal–electrolyte interfaces

To assess the sensitivity of optical readouts under electrochemical perturbation, we simulated the response of three label-free optical sensing techniques (NIRM, SPR, and LSPR) to voltage-induced refractive index changes across the electrical double layer. The model system, illustrated in Fig. 3a, included three voltage-sensitive regions: the TF layer representing electronic screening within the metal and two sub-domains of the diffuse layer in the electrolyte. All other layers were assigned fixed refractive indices, as detailed in the Methods section.

Optical responses were calculated using multilayer reflectance simulations for NIRM and SPR based on the transmission line model and Mie scattering theory for LSPR, as described in Sections S5 and S6. Fig. 4 presents the simulated optical response under three distinct scenarios: (1) refractive index changes confined to the TF layer, (2) changes confined to the diffuse layer (comprising the two sub-diffuse regions), and (3) combined contributions from both the TF and the diffuse layer. Each simulation was performed over an applied voltage range of ±200 mV, representing the typical regime of EDLC
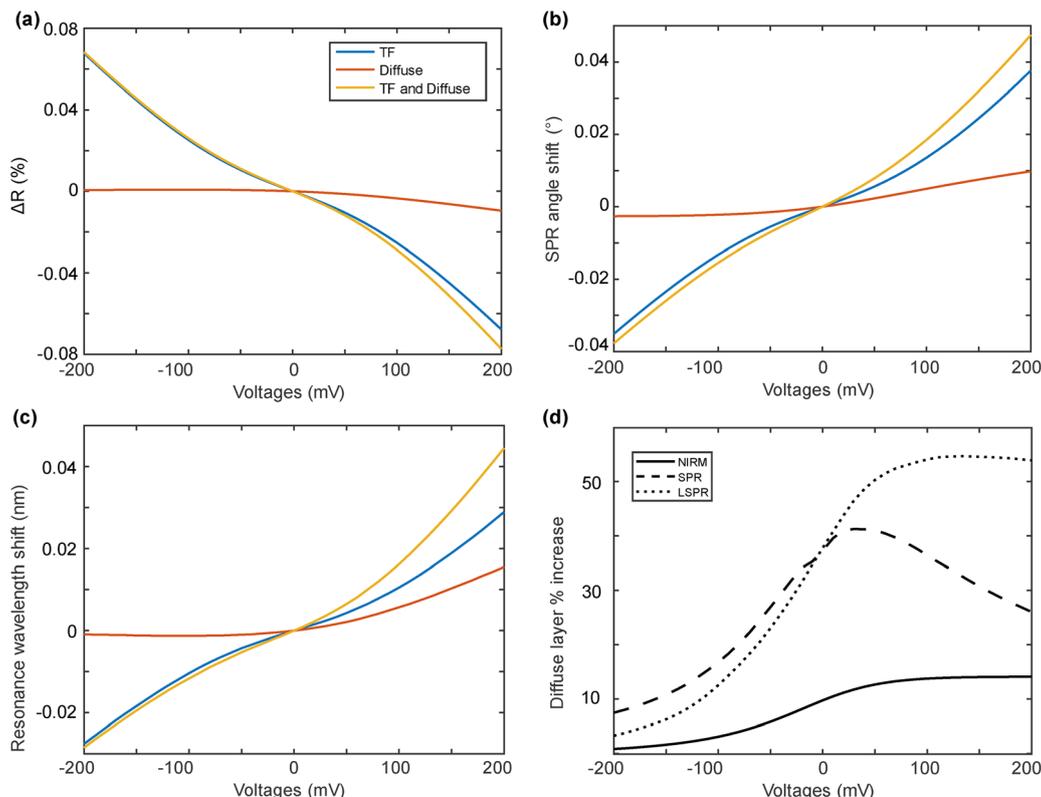
10858 | *Phys. Chem. Chem. Phys.*, 2026, **28**, 10853–10864

This journal is © the Owner Societies 2026

Fig. 4 Optical response of the electrode–electrolyte interface under voltage perturbation simulated for (a) NIRM, (b) SPR, and (c) LSPR sensing configurations. The total change in optical signal is decomposed into the contribution of the metal (only the TF region in blue), the diffuse layer (in red) and the combined contribution of both (in yellow). (d) The percentage increase in signal response due to the diffuse layer is calculated relative to the TF-only contribution for each technique across the voltage range, NIRM (solid line), SPR (dashed line), and LSPR (dotted line).

charging. It is important to note that all three sensing techniques, mentioned previously, demonstrate the ability to detect refractive index changes arising from EDLC modulation. However, they differ markedly in terms of sensitivity and field confinement. To compare their ability to resolve ionic contributions, the relative increase in optical response due to the diffuse layer was also quantified for each technique, as described below.

Normal-incidence reflection modulation (NIRM)

Fig. 4a shows reflectance modulation for the NIRM configuration at a wavelength of 640 nm, using a seven-layer model comprising BK7 glass, bulk gold, the TF layer, the Stern layer, two sub-diffuse layers, and the bulk electrolyte. The total reflectance changes range from –0.0774% to +0.0683% over ±200 mV. The dominant modulation arises from the TF layer, while the diffuse layer contributes up to ∼14% additional signal relative to the TF-only response at +200 mV. The TF-only signal is symmetric about 0 V, consistent with the linear dielectric behaviour of the free electron gas. Inclusion of the diffuse layer introduces visible asymmetry under positive bias, where chloride ions, due to their higher molar refractivity, accumulate near the surface and enhance the optical response. The diffuse-layer contribution remains modest in absolute terms (<0.01 percentage points) due to NIRM's infinite probing depth that extends to the bulk electrolyte and thus reduces spatial

specificity. This makes it less suited for sensitive detection of nanoscale charge rearrangements near the interface.

Surface plasmon resonance (SPR)

Fig. 4b presents the resonance angle shifts for a Kretschmann SPR configuration at 640 nm, using the same seven-layer structure. At 0 V, the baseline resonance angle is 74.1763°, while the ±200 mV range induces shifts from –0.0377° to +0.0474°. The TF region again dominates the response, but the diffuse layer enhances the total shift by up to ∼41%, at the positive voltage of 200 mV. At –200 mV, the contribution is smaller (∼7.5%), reflecting the lower refractive index of Na^+ compared to Cl^-, as shown in Fig. 4d. The SPR evanescent field depth is on the order of 100 nm,[45] providing a higher sensitivity to ionic redistribution within the diffuse layer when compared to the infinite field depth of NIRM. The asymmetric optical response of the technique, induced by ion-specific refractive index changes, enhances its utility for studying ion dynamics within the diffuse layer at electrode–electrolyte interfaces. This capability will further enhance the diverse applications of SPR in label-free biosensing and electrochemical investigations.

Localised surface plasmon resonance (LSPR)

Fig. 4c shows the resonance wavelength shift for LSPR using 50-nm diameter gold nanoparticles. Unlike NIRM and SPR, this

This journal is © the Owner Societies 2026

Phys. Chem. Chem. Phys., 2026, **28**, 10853–10864 | **10859**

model excludes the BK7 substrate. The voltage-induced shift spans from –0.285 nm to +0.445 nm, with the diffuse layer contributing up to ∼55% additional signal relative to the case that considers the TF-only region, as demonstrated in Fig. 4d. The field decay length in LSPR is limited to a region within ∼10 nm from the nanoparticle surface, as expected from the dipolar near-field profile, which decays with distance as $1/r^3$.[60] This strong spatial confinement localises the optical sensitivity to the zone where ionic gradients are steepest, making the technique highly responsive to near-surface changes. This confinement therefore enhances the polarity-dependent asymmetry, with Cl^- accumulation under positive bias producing much stronger shifts than the Na^+ response under negative potentials.

Cross-platform response to diffuse layer refraction modulation

To directly compare the relative impact of the diffuse layer on each sensing method, Fig. 4d reports the percentage increase in voltage-induced optical modulation due to the inclusion of the refractive index change of the diffuse layer. This was computed as follows:

$$\% \text{ Increase} = \left(\frac{\Delta_{\text{(TF+Diffuse)}}}{\Delta_{\text{TF}}} - 1 \right) \times 100 \qquad (8)$$

where $\Delta_{\text{(TF+Diffuse)}}$ represents the total change in both TF and diffuse layers with respect to 0 V for each technique. The maximum increases were ∼14% for NIRM, ∼41% for SPR, and ∼55% for LSPR at +200 mV. In all cases, the enhancement is asymmetric, with higher values at positive voltages due to the stronger contribution of chloride ions.

These results confirm that although all three techniques can sense voltage-induced refractive index changes in the EDLC, their sensitivity to ionic processes depends strongly on the field decay length at the sensor's interface. NIRM integrates a weak ionic signal over an infinite penetration depth, while SPR sensors have a short penetration depth on the order of 100 nm and therefore provide a higher sensitivity. LSPR has the smallest penetration depth and demonstrates the highest sensitivity at detecting local ionic redistribution. These findings could inform sensor design where the penetration depth and field enhancement play a key role in sensitive detection of ions at sensing interfaces.

While our study has focused primarily on gold as a sensor material, other metals and semiconductors can be explored for use in wide-ranging applications. This requires exploring advanced solid-state physics models[61–64] to estimate charge-carrier density dynamics during electrochemical processes.

Beyond dilute-electrolyte low-field regimes

This work targets a parameter regime in which classical PB/PNP descriptions of EDL remain quantitatively reliable. Specifically, the analysis deliberately focuses on the dilute low-voltage regime (0.15 M, ±0.2 V) with a fixed 0.5 nm ion-free Stern layer, where PB/PNP descriptions are expected to remain quantitatively reliable and the response is strictly non-faradaic.

A broad range of theoretical work addresses non-classical electrical double-layer behaviour that emerges at high ionic strength and under strong interfacial fields. Correlation-aware continuum models developed for ionic liquids and concentrated electrolytes capture overscreening, crowding, and interfacial layering effects that lie outside the dilute-solution window considered here (*e.g.* Bazant–Storey–Kornyshev-type frameworks[65]). Hydration-mediated and finite-size PB extensions introduce soft, ion-specific repulsions and steric constraints that regulate counter-ion densities and reproduce layering and overcharging at higher $|V|$ or with multivalent ions.[66,67] Similarly, PB–Lennard-Jones formulations show that dispersion and soft repulsion primarily affect the interfacial structure at elevated concentrations, with ion–ion dispersion negligible at ≤1 M.[68] Furthermore, the study of the optical properties of the EDLC could utilise input from quantum and semiclassical models of complex electrochemical interfaces.[69–71] While such advanced models are not required for the present scope, future extensions could incorporate steric regularisation of the diffuse layer or correlation-dependent permittivity profiles $\varepsilon(x)$ as a baseline for optical modelling, potentially refining refractive-index predictions without altering the main conclusions. Another crucial aspect of these advanced approaches concerns the influence on ionic molar refractivity near charged surfaces, particularly in scenarios involving overscreening, crowding, and the impact of the ion size. Ion–ion interactions are anticipated to cause deviations from the theoretical refractivity values calculated for dilute concentrations, thereby requiring corrections to accurately assess the refractive index dynamics of EDLCs in ionic liquids.

Conclusions

This study presents a computational framework to disentangle the individual contributions of cations and anions to refractive index changes in EDLCs, enabling the development of label-free methods for sensing charge transport. Coupled electrodiffusion–electrostatics modelling and optical multilayer simulations of metal–electrolyte interfaces show that optical responses from NIRM, SPR, and LSPR arise from distinct contributions of ionic species. Cations and anions contribute unequally due to their differing molar refractivities; in sodium chloride, chloride ions dominate, creating a marked asymmetry under polarity switching that signals cation *versus* anion accumulation.

Each technique probes different physical aspects of the EDLC. NIRM, with the infinite penetration depth extending to the bulk electrolyte, is relatively less sensitive to nanoscale ionic redistribution. SPR, with ∼100 nm evanescent decay, detects both thin-film and diffuse-layer contributions but retains the bulk background. LSPR, with ∼10 nm near-field decay, is most sensitive to ionic redistribution in the ∼2 nm diffuse layer where the optical field is most confined. This field–confinement relationship is key for optimised sensor design.

Our quantitative framework predicts label-free optical sensor performance and can be extended to non-planar interfaces to better capture biological and energy-related conditions.

10860 | *Phys. Chem. Chem. Phys.*, 2026, **28**, 10853–10864

This journal is © the Owner Societies 2026

Discriminating ionic species by molecular refractivity offers a pathway for monitoring ion dynamics in electrochemical and cellular systems where selectivity matters.

Methods

Finite-element modelling using COMSOL

The model consists of a one-dimensional half-cell that is 100 nm in length, divided into two domains representing the Stern layer adjacent to the electrode and the transition from the interface to the bulk electrolyte. As mentioned previously, the Stern layer thickness, equivalent to the distance to the outer Helmholtz plane, was set to 0.5 nm for both ionic species. The total model length was chosen to be much larger than the TF screening length, ensuring that the concentration and potential fields were not affected by the boundary conditions imposed at the bulk interface. A constant relative permittivity of water, $\varepsilon_r = 78$, was assumed throughout the electrolyte domain, regardless of the concentration.

Boundary conditions were defined as follows:

• At the electrode surface ($x = 0$), the electric potential was set to V_{in} and the normal ionic flux was constrained to zero.

• At the bulk boundary ($x = 100$ nm), the potential was fixed at 0 V, and the ionic concentrations were held at 150 mM, allowing ionic currents to maintain equilibrium.

• Within the Stern layer ($0 < x < 0.5$ nm), both cation and anion concentrations were set to 0 M, with zero volumetric charge density. This region is treated as a layer of solvated water molecules without free ions; however, electric potential can still drop across it.

• At the interface between the Stern and diffuse layers, ionic flux was set to zero, reflecting the physical limit of closest approach for solvated ions.

The electrostatics and ion transport problems were coupled *via* bi-directional interaction between the electrostatics and transport of diluted species physics interfaces in COMSOL Multiphysics. The mesh resolution was set to 0.16 nm in the Stern layer based on convergence studies and 0.1 nm elsewhere, ensuring fine resolution of the electric double layer without incurring prohibitive computation time due to the one-dimensional geometry. Simulations were conducted over a voltage range of ±200 mV, with output data including potential, electric field, and ionic concentration profiles used for post-processing and optical modelling. This voltage window was selected to ensure a non-faradaic, linear-dielectric regime in which mean-field EDLC theory remains valid.

Modelling of refractive index changes at the metal–electrolyte interface

The change in refractive index at the metal–electrolyte interface was modelled based on the excess polarizability induced by voltage-driven redistribution of ionic species in the diffuse layer. As ions accumulate or are depleted near the interface, depending on the applied voltage polarity, the local dielectric environment changes, giving rise to a spatial gradient in the refractive index. This effect was quantified using Lorenz–Lorentz eqn (1), adapted for multicomponent mixtures, excluding specific adsorption, previously introduced in the introduction with derivation provided in Section S1.

To calculate the voltage-dependent refractive index in the diffuse layer, ion concentration profiles were extracted from finite-element simulations for applied voltages on the order of ±200 mV in 10 mV steps. These profiles were analysed within two spatial regions beyond the Stern layer:

• The first sub-diffuse layer (0.5–1.3 nm), which corresponds to the Debye length where the potential decays to $1/e$ of its value at the Stern boundary and

• The second sub-diffuse layer (1.3–2.1 nm), where the potential further decays to approximately $1/e^2$.

These boundaries are not a universal standard, but rather a convenient framework to simplify the optical model into two effective layers beyond the gold interface. In the standard description, the diffuse layer is treated as one continuous region extending into the electrolyte.

For each voltage, the surface ion concentration in each sublayer was calculated by numerically integrating the simulated profiles over the corresponding spatial range. These values were converted into volumetric concentrations by dividing by the sublayer thickness (0.7 nm), which corresponds to the theoretical Debye length, $1/\kappa$, derived from the exponential decay of potential in the diffuse layer:[51]

$$\phi = \phi_S e^{-\kappa x} \tag{9}$$

$$\kappa = \sqrt{\frac{2c_0 z^2 e^2}{\varepsilon \varepsilon_0 kT}} \tag{10}$$

where ϕ_S is the Stern potential, c_0 is the bulk ion concentration, z is the valency, e is the elementary charge, ε_0 and ε are the permittivity of free space and water, respectively, and kT is the thermal energy. This formulation applies to symmetric $z:z$ electrolytes, such as NaCl used in this study.

The local refractive index at position x was then computed as follows:

$$n(x) = n_{H_2O} + \beta[R_{Na^+} \cdot c_{Na^+}(x) + R_{Cl^-} \cdot c_{Cl^-}(x)] \tag{11}$$

with $n_{H_2O} = 1.3316$ (at 640 nm)[72] and molar refractivity $R_{Na^+} = 0.65 \times 10^{-6}$ m^3 mol^{-1} and $R_{Cl^-} = 8.57 \times 10^{-6}$ m^3 mol^{-1}.[44,59] The value $\beta = 1.78$ was used, as derived in eqn (S1.7). The ion concentration $c_i(x)$ for each ion was calculated using COMSOL as mentioned above. The refractive index deviation due to excess polarizability was obtained by subtracting both the water and bulk ionic contributions, as described in eqn (3). This process was implemented in MATLAB, directly using concentration profiles obtained from COMSOL simulations and calculating the refractive index response pointwise for each voltage value. Separate contributions from Na$^+$ and Cl$^-$ were also calculated to analyse their individual optical effects across the voltage range.

This journal is © the Owner Societies 2026

Phys. Chem. Chem. Phys., 2026, **28**, 10853–10864 | **10861**

Modelling the optical response of NIRM, SPR and LSPR configurations

The models employed in this work calculate the voltage and refractive index induced changes in the output of three sensing techniques as described below. To investigate this effect, we calculated the change in reflectivity for a NIRM configuration, the resonance angle shift for a Kretschmann–Raether SPR sensing configuration and the resonance wavelength shift for LSPR sensing. All these approaches account for variations induced by the voltage-dependent refractive index changes in the TF layer and the diffuse layer of the electrical double layer.

To investigate voltage sensing using NIRM and SPR configurations, we employed the transmission line approach, as described by Somekh *et al.*[73] and detailed in Section S5. This method uses the concept of impedance, a well-established framework in optical and microwave engineering, to characterise the behaviour of reflected light interacting with layered structures. The approach was chosen for its computational efficiency compared to the transfer matrix method (TMM), particularly for systems with multiple layers.[73] By avoiding computationally intensive matrix operations, the transmission line method provides an accurate and efficient means of modelling the optical response. To investigate voltage-modulated scattering by plasmonic nanoparticles, we used a Mie scattering model, described in detail in Section S6, which accounts for the changes in refractive index at the nanoparticle–electrolyte interface.

NIRM configuration

For the NIRM configuration, we analysed a seven-layered system consisting of a semi-infinite glass BK7 substrate ($n = 1.5148$, fixed[74]), a 20 nm bulk gold layer ($n = 0.30409 + 3.2093i$, fixed[75]), a 0.058 nm TF layer (voltage-dependent refractive index, described in ref. 24), a 0.5 nm Stern layer ($n = 1.33156$, matching pure water, fixed[72]), 1st and 2nd sub-diffuse layers (0.7829 nm thickness, voltage-dependent refractive index) and a semi-infinite bulk electrolyte (150 mM NaCl, $n = 1.3315614$, fixed). The simulation was performed using a 640 nm light source emerging from the glass medium at $0°$ incidence. Using the transmission line model described in Section S5, we calculated the changes in the total multilayer reflectance across a voltage range of ± 200 mV. Reflectance is defined as $R = |r_\text{p}|^2 \times 100$, where r_p is the reflection coefficient for p-polarization, and the change is defined as $\Delta R = R$ (at a given voltage) $- R_0$ (at 0 V). These changes result from the voltage-induced refractive index variations in the TF and sub-diffuse layers relative to the 0 V case. The 0 V case is modelled as a simplified four-layer structure consisting of glass, bulk gold, a Stern layer, and a bulk electrolyte.

SPR configuration

For the SPR voltage sensing, we simulated the SPR curve for the seven-layer system described in the previous paragraph, with a modification that involved using a 50 nm bulk gold layer instead of 20 nm. The SPR curve was obtained by calculating the reflectance using the transmission line model, incorporating variations in the angle of incidence from 70 to $75°$ at steps of 1×10^{-5} degrees. To determine the resonance angle, the minimum reflectance was identified using the min function in MATLAB and associated with its corresponding angle of incidence. A resonance angle of $74.17629°$ corresponds to 0 V when using a simplified four-layered system (glass/bulk gold/Stern layer/bulk electrolyte) while maintaining the refractive index values from the seven-layer system described in the previous section. By incorporating the voltage-dependent refractive index variations for the seven-layered system, we determined the resonance angle shift over a voltage range of ± 200 mV by computing the resonance angle for the voltage-applied case and subtracting the resonance angle at 0 V ($\Delta\theta = \theta_\text{SPR}$ (at a given voltage) $- \theta_\text{SPR,0}$ at 0 V). The SPR angle variation was calculated with a resolution of 10^{-5} degrees.

LSPR configuration

To simulate voltage-dependent optical scattering by plasmonic nanoparticles, we used a multilayered Mie scattering model based on concentric spherical domains. The model evaluates shifts in resonance wavelength resulting from voltage-induced refractive index changes in both the particle and surrounding electrolyte. Full details of the model and implementation are provided in Section S6.

We modelled gold nanoparticles using concentric layers representing (i) a bulk gold core with wavelength-dependent permittivity,[75] (ii) a TF screening layer (thickness = 0.058 nm) with voltage-dependent permittivity derived from the Drude model,[24] (iii) a Stern layer (thickness = 0.5 nm and refractive index = 1.33156[72]), (iv) two voltage-dependesnt sub-diffuse layers (thickness of each = 0.7829 nm), and (v) a semi-infinite bulk electrolyte; calculations are discussed in the previous section.

Scattering was calculated using the scattnlay function,[76] which evaluates Mie coefficients for multilayered spheres. The model computes extinction, scattering, and absorption efficiencies across the 400–800 nm range in 1 nm steps to identify the unperturbed resonance peak. A refined evaluation in 1 Å steps around this peak was then used to track voltage-induced resonance shifts at ± 200 mV in 1 mV increments.

Our application accounts for charge-dependent optical properties that occur both within the TF layer of the particle and within the surrounding diffuse layer of the electrolyte medium. To illustrate the significance of these phenomena, we implemented three model variations:

1. Particle-only modulation: Only the refractive index of the particle's TF layer varies with voltage; the surrounding medium is fixed.

2. Electrolyte-only modulation: The particle refractive index is held constant, while those of the electrolyte's diffuse layers vary according to simulated ion redistribution and molar refractivity.

3. Combined system: The refractive indices of both the TF layer and diffuse electrolyte are voltage-responsive.

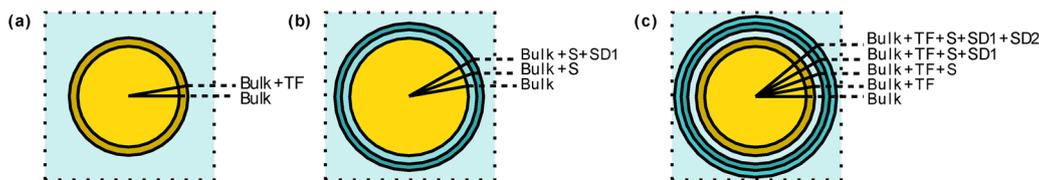A schematic representation of the multilayer geometry used in each case is shown in Fig. 5.

10862 | *Phys. Chem. Chem. Phys.*, 2026, **28**, 10853–10864

This journal is © the Owner Societies 2026

Fig. 5 Schematic representation of three optical models for nanoparticles: (a) charge screening within the particle, (b) ionic redistribution in the electrolyte, and (c) combined effects of both mechanisms. Layer abbreviations: bulk, TF length, Stern layer (S), and sub-diffuse regions (SD1 and SD2).

Author contributions

K. R. M. conceptualized the study, developed the models for analysing the refractive index changes in the diffuse layer, performed data analysis, and produced figures. F. N. contributed to modelling by performing the optical simulations for LSPR. W. H. carried out the electrodiffusion modelling in COMSOL. K. R. M. and S. A. drafted the manuscript, and F. N. and W. H. contributed to the writing of the manuscript. R. F. D. supervised the project and contributed to the editing of the manuscript. M. S. supervised the project and provided critical input on data interpretation. S. A. conceptualized the study, developed the theory, supervised the project, and edited the manuscript. All authors discussed the results and reviewed the manuscript.

Conflicts of interest

There are no conflicts to declare.

Data availability

The data that support the findings of this study were generated computationally and are available from the corresponding author upon reasonable request. This includes COMSOL Multiphysics model files, MATLAB scripts for refractive index calculations and optical simulations, and all numerical datasets used in figures.

Acknowledgements

References

1 Y. Zhang, T. Sun, X. Yang, L. Zhou, C. M. J. Tan, M. Lei and H. Bayley, *Nat. Chem. Eng.*, 2024, **1**, 691–701.

2 R. O'Hayre, S. Cha, W. Colella and F. B. Prinz, *Fuel Cell Fundamentals*, John Wiley & Sons, Hoboken, NJ, 2016.

3 G. Ertl, H. Knözinger and J. Weitkamp, *Handbook of Heterogeneous Catalysis*, Wiley-VCH, Weinheim, 2008.

4 R. W. Revie and H. H. Uhlig, *Corrosion and Corrosion Control: An Introduction to Corrosion Science and Engineering*, Wiley, Hoboken, NJ, 4th edn, 2008.

5 Z. Schofield, G. N. Meloni, P. Tran, C. Zerfass, G. Sena, Y. Hayashi, M. Grant, S. A. Contera, S. D. Minteer, M. Kim, A. Prindle, P. Rocha, M. B. A. Djamgoz, T. Pilizota, P. R. Unwin, M. Asally and O. S. Soyer, *J. R. Soc., Interface*, 2020, **17**, 20200013.

6 A. R. Pereira, G. C. Sedenho, J. C. P. de Souza and F. N. Crespilho, *An. Acad. Bras. Cienc.*, 2018, **90**, 825–857.

7 A. T. Yahiro, S. M. Lee and D. O. Kimble, *Biochim. Biophys. Acta*, 1964, **88**, 375–383.

8 P. Das, M. Das, S. R. Chinnadayyala, I. M. Singha and P. Goswami, *Biosens. Bioelectron.*, 2016, **79**, 386–397.

9 Z. Hemmatian, S. Keene, E. Josberger, T. Miyake, C. Arboleda, J. Soto-Rodríguez, F. Baneyx and M. Rolandi, *Nat. Commun.*, 2016, **7**, 12981.

10 J. Wünsche, Y. Deng, P. Kumar, E. Di Mauro, E. Josberger, J. Sayago, A. Pezzella, F. Soavi, F. Cicoira, M. Rolandi and C. Santato, *Chem. Mater.*, 2015, **27**, 436–442.

11 Y. Deng, E. Josberger, J. Jin, A. Fadavi Roudsari, B. A. Helms, C. Zhong, M. P. Anantram and M. Rolandi, *Sci. Rep.*, 2013, **3**, 2481.

12 F. J. Rawson, C. L. Yeung, S. K. Jackson and P. M. Mendes, *Nano Lett.*, 2013, **13**, 1–8.

13 A. J. Robinson, A. Jain, H. G. Sherman, R. J. M. Hague, R. Rahman, P. Sanjuan-Alberte and F. J. Rawson, *Adv. Ther.*, 2021, **4**, 2000248.

14 K. F. Chow, F. Mavré, J. A. Crooks, B. Y. Chang and R. M. Crooks, *J. Am. Chem. Soc.*, 2009, **131**, 8364–8365.

15 A. Jain, J. Gosling, S. Liu, H. Wang, E. M. Stone, S. Chakraborty, P.-S. Jayaraman, S. Smith, D. B. Amabilino, M. Fromhold, Y.-T. Long, L. Pérez-García, L. Turyanska, R. Rahman and F. J. Rawson, *Nat. Nanotechnol.*, 2024, **19**, 106–114.

16 C. L. Bentley, J. Edmondson, G. N. Meloni, D. Perry, V. Shkirskiy and P. R. Unwin, *Anal. Chem.*, 2019, **91**, 84–108.

17 L. Bouffier, D. Zigah, N. Sojic and A. Kuhn, *Annu. Rev. Anal. Chem.*, 2021, **14**, 65–86.

18 X. Shan, U. Patel, S. Wang, R. Iglesias and N. Tao, *Science*, 2010, **327**, 1363–1366.

19 A. J. Merryweather, C. Schnedermann, Q. Jacquet, C. P. Grey and A. Rao, *Nature*, 2021, **594**, 522–528.

20 S. A. Abayzeed, *Biomed. Opt. Express*, 2020, **11**, 6168–6180.

21 V. Brasiliense, A. N. Patel, A. Martinez-Marrades, J. Shi, Y. Chen, C. Combellas, G. Tessier and F. Kanoufi, *J. Am. Chem. Soc.*, 2016, **138**, 3478–3483.

This journal is © the Owner Societies 2026

Phys. Chem. Chem. Phys., 2026, **28**, 10853–10864 | **10863**

22 D. Valavanis, P. Ciocci, I. J. McPherson, G. N. Meloni, J. F. Lemineur, F. Kanoufi and P. R. Unwin, *ACS Electrochem.*, 2025, **1**, 153–163.

23 W. R. Heineman, *Anal. Chem.*, 1978, **50**, 390A–402A.

24 S. A. Abayzeed, R. J. Smith, K. F. Webb, M. G. Somekh and C. W. See, *Opt. Express*, 2017, **25**, 31552–31567.

25 R. Kötz and D. M. Kolb, *Z. Phys. Chem.*, 1978, **112**, 69–83.

26 R. P. Howson, J. Avaritsiotis and T. Fox, *Thin Solid Films*, 1975, **30**, 297–309.

27 M. Celebrano, C. Sciascia, G. Cerullo, M. Zavelani-Rossi, G. Lanzani and J. Cabanillas-Gonzalez, *Adv. Funct. Mater.*, 2009, **19**, 1180–1185.

28 K. Maize, A. Kundu, G. Xiong, K. Saviers, T. S. Fisher and A. Shakouri, *Analyst*, 2016, **141**, 1448–1461.

29 K. J. Foley, X. Shan and N. J. Tao, *Anal. Chem.*, 2008, **80**, 5146–5151.

30 K. Namink, X. Meng, M. T. M. Koper, P. Kukura and S. Faez, *Phys. Rev. Appl.*, 2020, **13**, 044065.

31 Y. Zhang, M. Nguyen, C. Schnedermann, S. T. Keene, I. Jacobs, A. Rao and H. Sirringhaus, *J. Chem. Phys.*, 2023, **158**, 034201.

32 J. Dong, Y. Lu, Y. Xu, F. Chen, J. Yang, Y. Chen and J. Feng, *Nature*, 2021, **596**, 244–249.

33 Q.-Y. Li, P.-T. Lyu, B. Kang, H.-Y. Chen and J.-J. Xu, *Nat. Photonics*, 2025, **19**, 871–878.

34 T. Liu, M. Li, Y. Wang, Y. Fang and W. Wang, *Chem. Sci.*, 2018, **9**, 4424–4429.

35 Z. Zhang, J. Yang, C. Lian and S. Faez, *J. Phys. D: Appl. Phys.*, 2021, **54**, 384005.

36 Z. Zhang and S. Faez, *Faraday Discuss.*, 2023, **246**, 426–440.

37 H. Kragh, *Substantia*, 2018, **2**, 7–18.

38 Y. Liu and P. H. Daum, *J. Aerosol Sci.*, 2008, **39**, 974–986.

39 P. Pacák, *Chem. Pap.*, 1989, **43**, 489–500.

40 F. Booth, *J. Chem. Phys.*, 1951, **19**, 391–394.

41 R. Bouteloup and D. Mathieu, *Phys. Chem. Chem. Phys.*, 2018, **20**, 22017–22026.

42 L. C. Pauling, *Proc. R. Soc. London, Ser. A*, 1927, **114**, 181–211.

43 F. H. Newman, *Philos. Mag.*, 1934, **17**, 1072–1075.

44 Y. Marcus, *Ion Properties*, Marcel Dekker, New York, 1997, ch. 6, pp. 87–96.

45 D. Kim and S. J. Yoon, *J. Opt. Soc. Am. A*, 2007, **24**, 2543–2549.

46 A. J. Haes and R. P. Van Duyne, *Anal. Bioanal. Chem.*, 2004, **379**, 920–930.

47 X. Yang and G. Zhang, *Nanotechnology*, 2007, **18**, 335201.

48 R. Morrow, D. R. McKenzie and M. M. M. Bilek, *J. Phys. D: Appl. Phys.*, 2006, **39**, 937–943.

49 Y. Shi, G. Feng, X. Li, X. Yang, A. H. Ghanim, P. Ruchhoeft, D. Jackson, S. Mubeen and X. Shan, *Anal. Chem.*, 2021, **93**, 12320–12328.

50 J. Yang, A. Gallegos, C. Lian, S. Deng, H. Liu and J. Wu, *Chin. J. Chem. Eng.*, 2021, **31**, 145–152.

51 A. J. Bard and L. R. Faulkner, *Electrochemical Methods: Fundamentals and Applications*, John Wiley & Sons, New York, NY, 2nd edn, 2001, ch. 13, pp. 534–556.

52 J. Homola, *Chem. Rev.*, 2008, **108**, 462–493.

53 K. Thadson, S. Sasivimolkul, P. Suvarnaphaet, S. Visitsattapongse and S. Pechprasarn, *Sci. Rep.*, 2022, **12**, 2052.

54 G. Moon, J. Lee, H. Lee, H. Yoo, K. Ko, S. Im and D. Kim, *Cell Rep. Phys. Sci.*, 2022, **3**, 101042.

55 G. Moon, T. Son, H. Lee and D. Kim, *Anal. Chem.*, 2019, **91**, 9538–9545.

56 R. W. Taylor and V. Sandoghdar, *Nano Lett.*, 2019, **19**, 4827–4835.

57 D. Cole, G. Young, A. Weigel, A. Sebesta and P. Kukura, *ACS Photonics*, 2017, **4**, 211–216.

58 R. W. Taylor, R. G. Mahmoodabadi, V. Rauschenberger, A. Giessl, A. Schambony and V. Sandoghdar, *Nat. Photonics*, 2019, **13**, 480–487.

59 V. K. Laurinavichyute, S. Nizamov and V. M. Mirsky, *Chem. Phys. Chem.*, 2017, **18**, 1552–1560.

60 S. A. Maier, *Plasmonics: Fundamentals and Applications*, Springer, New York, 2007, pp. 66–71.

61 S. Wang, N. T. Hung, H. Tian, M. S. Islam and R. Saito, *Phys. Rev. Appl.*, 2021, **16**, 024030.

62 P. Abudu and Y. He, *Electrochim. Acta*, 2025, **524**, 145998.

63 L. Scalfi, M. Salanne and B. Rotenberg, *Annu. Rev. Phys. Chem.*, 2021, **72**, 189–212.

64 D. Jacob and J. J. Palacios, *J. Chem. Phys.*, 2011, **134**, 044118.

65 M. Z. Bazant, B. D. Storey and A. A. Kornyshev, *Phys. Rev. Lett.*, 2011, **106**, 046102.

66 M. A. Brown, G. V. Bossa and S. May, *Langmuir*, 2015, **31**, 11477–11483.

67 A. Gupta, A. Govind Rajan, E. A. Carter and H. A. Stone, *Phys. Rev. Lett.*, 2020, **125**, 188004.

68 A. Seal, U. Tiwari, A. Gupta and A. G. Rajan, *Phys. Chem. Chem. Phys.*, 2023, **25**, 21708–21722.

69 Z. Zhang and J. Huang, *JACS Au*, 2025, **5**, 3453–3467.

70 N. R. Agrawal, C. Duan and R. Wang, *J. Phys. Chem. B*, 2024, **128**, 303–311.

71 J. Wu, *Chem. Rev.*, 2022, **122**, 10821–10859.

72 A. N. Bashkatov and E. A. Genina, in Saratov Fall Meeting 2002: Optical Technologies in Biophysics and Medicine IV, *Proc. SPIE*, 2003, vol. 5068, pp. 393–395.

73 M. G. Somekh, K. Regules-Medel and S. A. Abayzeed, *J. Opt. Soc. Am. A*, 2024, **41**, C90–C98.

74 M. N. Polyanskiy, *Sci. Data*, 2024, **11**, 94.

75 A. D. Rakić, A. B. Djurišić, J. M. Elazar and M. L. Majewski, *Appl. Opt.*, 1998, **37**, 5271–5283.

76 O. Peña and U. Pal, *Comput. Phys. Commun.*, 2009, **180**, 2348–2354.

10864 | *Phys. Chem. Chem. Phys.*, 2026, **28**, 10853–10864

This journal is © the Owner Societies 2026